




Cite this: DOI: 10.1039/d5sc03046c

 All publication charges for this article have been paid for by the Royal Society of Chemistry

# Unraveling plating/stripping-induced strain evolution *via* embedded sensors for predictive failure mitigation in solid-state Li metal batteries

Hongye Zhang,<sup>a</sup> Zhipeng Chen,<sup>a</sup> Xinren Zhang,<sup>b</sup> Ziyi Shen,<sup>a</sup> Fei Xu <sup>\*b</sup> and Fenghui Wang<sup>\*a</sup>

Solid-state lithium metal batteries represent a critical frontier in energy storage technology, yet persistent interfacial instability between the Li metal anode and solid electrolytes generates detrimental electrochemical–mechanical interactions that undermine the cycling durability. To resolve this fundamental challenge, herein, we establish an innovative real-time strain monitoring that directly correlates micro-mechanical evolution with interfacial degradation during Li plating/stripping. It reveals that Li plating induces significant microstrain accumulation, while stripping processes only partially release mechanical stress. Systematic analysis identifies three characteristic strain evolution periods during cycling: initial linear growth, intermediate stabilization, and terminal exponential escalation prior to cell failure. Post-mortem characterization attributes the final strain surge to synergistic cumulative dendrite propagation, dead lithium agglomeration, and SEI disintegration. Parametric studies demonstrate that an elevated cell stack pressure from 200 KPa to 3500 KPa reduced the initial strain growth cycle by 50% and stabilized the strain value by 47.4%, whereas doubling the current density prolongs the 10-fold linear growth period and increases the 4-fold plateau strain one, severely curtailing battery longevity. Crucially, we establish predictive correlations between strain trajectory patterns and electrochemical failure signature. This mechano-analytical platform enables non-destructive interrogation of interfacial dynamics, providing an operational protocol for failure diagnosis and pressure-current parameter optimization to achieve durable solid-state battery systems.

Received 26th April 2025  
Accepted 29th July 2025

DOI: 10.1039/d5sc03046c

rsc.li/chemical-science

## Introduction

Currently, the development of both energy-dense and safe rechargeable battery technologies is highly desirable but remains to be a longstanding challenge, owing to the well-known trade-off between the activity and stability of electrode materials.<sup>1,2</sup> Solid-state lithium metal batteries are anticipated to meet the demands for large specific energy density and high safety, due to the inherent advantages of high capacity and low redox potential of Li metal and the non-flammable nature of solid electrolytes.<sup>3–5</sup> However, the unstable Li metal anode/solid-state electrolyte interface critically restricts the state-of-the-art Li metal batteries. Specifically, the repeated and inhomogeneous deposition and dissolution of the Li anode, coupled with the spontaneous formation of an unstable solid electrolyte interface (SEI), gives rise to uncontrollable morphological

evolution,<sup>6,7</sup> thus dramatically sacrificing the energy density and cycling life and posing serious safety hazards.<sup>8–10</sup> All-solid-state batteries utilizing high mechanical strength solid-state electrolytes could enhance the safety by eliminating fire hazards.<sup>11</sup> However, the intrinsic weak solid–solid contact and interface instabilities have hindered the development of all-solid-state batteries.<sup>12,13</sup> In contrast to the liquid electrolyte that could mitigate electrochemical Li plating/stripping induced strain with soft liquids, the stresses and strains generated in solid-state battery configuration can be transferred more obviously. Consequently, the phenomenon of electrochemical–mechanical coupling becomes more severe and exaggerated in solid-state battery systems. Manifesting the electric–electrochemical–mechanical mutual-coupling effect to the degradation mechanism is of great significance. On one hand, the mechanical strain generated by the intrinsic electrochemical Li plating/stripping can serve as an indicator to effectively monitor the battery service condition and failure evidence. Furthermore, based on mechanical–electrochemical coupling principles, there is a wealth of opportunities to establish optimal operating conditions (potential, current density, capacity, *etc.*) for charging and discharging, and meanwhile to pre-compensate or reduce the stresses within cells to extend the battery life and

<sup>a</sup>Department of Engineering Mechanics, Bio-Inspired and Advanced Energy Research Center, Northwestern Polytechnical University, Xi'an 710129, Shaanxi, China. E-mail: fhwang@nwpu.edu.cn

<sup>b</sup>State Key Laboratory of Solidification Processing, Center for Nano Energy Materials, School of Materials Science and Engineering, Northwestern Polytechnical University, China. E-mail: feixu@nwpu.edu.cn



safety. Therefore, clarifying the *ex/in situ* tracking of the microscopic morphology and structure of the lithium deposition/dissolution process, especially the interaction between the mechanical, electric and electrochemical fields, is of more significance for promoting the development of solid-state batteries.

Various advanced techniques have been employed to characterize the morphology, composition, and structure of Li surfaces, in pursuit of manifesting clear mechanisms for the formation and growth of Li dendrites.<sup>14</sup> Post-mortem disassembly of batteries is a widely used method for battery failure analysis. Optical microscopy, scanning electron microscopy (SEM), transmission electron microscopy (TEM), and atomic force microscopy (AFM) directly reveal high-resolution information on Li dendrite growth.<sup>15–18</sup> The Li deposition/stripping process is an interfacial reaction, and *ex situ* characterization may disrupt its original precise morphology. In particular, *in situ* analytical methods have greatly facilitated the understanding of lithium deposition mechanisms. *In situ* X-ray microtomography enables quantification of the porosity and volume fraction of Li deposits and circulating Li metal anodes.<sup>19</sup> Li-NMR spectroscopy provides *in situ* structural changes in Li metal during electrochemical cycling.<sup>20</sup> XRD can reveal the crystallographic orientation of Li deposits.<sup>21</sup> Neutron Depth Profiling (NDP) and Neutron Scattering methods provide non-destructive, highly sensitive analysis of the Li concentration and pore morphology.<sup>22</sup> Such non-destructive inspection of Li plating is quite important in practical battery systems, while there are no signals such as voltage and current that can be easily obtained,<sup>23</sup> and they often fall short in providing insights into mechanical properties. The construction of embedded sensors to *in situ* monitor the micromechanical change becomes a burgeoning new area of research.<sup>24–26</sup> However, these studies with embedded sensors primarily focused on liquid electrolyte systems, rather than all-solid-state battery systems. Consequently, there is an urgent need for developing *in situ* strain monitoring techniques to analyse force signals coupled with voltage and current responses for failure diagnosis in all-solid-state lithium metal batteries, which could be adaptable to integrate into electric vehicle battery management systems.<sup>27,28</sup>

This study presents a novel non-destructive strain measurement method for solid-state Li metal batteries, employing embedded strain gauge techniques to *in situ* monitor dynamic physical deformations during Li plating/stripping in half-cells. Our measurement principle relies on the precise detection of surface micro-deformations through resistive strain gauges, which offer exceptional accuracy ( $\pm 0.1 \mu\epsilon$  resolution) and sensitivity (gauge factor  $\approx 2.0$ ) for real-time monitoring of Li deposition-induced strains at the Cu current collector. It is observed that Li plating induces significant microstrain accumulation, while stripping processes only partially release mechanical stress in the starting cycles. Three distinct strain evolution periods were identified during continuous cycling, including initial linear growth, intermediate stabilization, and terminal exponential escalation prior to cell failure. Elevated stack pressures effectively delay strain progression during the

primary period, whereas increased current densities accelerate mechanical degradation throughout the entire cycling process. These findings establish strain monitoring as a powerful tool for assessing interfacial stability and degradation mechanisms in solid-state batteries.

## Results and discussion

### Principle of strain sensor monitoring for Li plating/stripping

To investigate the strain response during Li plating and stripping, we conducted strain measurements on solid-state Cu||Li half-cells assembled in the laboratory. The cell configuration consists of Cu foil as the working electrode, Li foil as the metal counter/reference electrode, and a PVDF-HFP/LLZTO composite solid-state electrolyte. Fig. 1 illustrates the principle of real-time strain monitoring during battery cycling. During the discharge (plating) process, Li ions from the negative electrode deposit onto the Cu foil, generating a tensile strain at the Cu foil's bottom surface. This causes the foil to bend away from the Li electrode, a deformation quantitatively recorded by the strain gauge. However, the limited intrinsic Li diffusion rate ( $<10^{-11} \text{ cm}^2 \text{ s}^{-1}$ ) leads to the formation of voids at the interface.<sup>29–31</sup> These voids accumulate over time, distorting the local electric field distribution and exacerbating heterogeneous Li plating in the adjacent region, ultimately triggering dendrite growth upon continuous cycling.<sup>32,33</sup> During the charge process, the deposited Li on Cu foil will strip away, leaving behind the “dead Li” from the as-generated dendrites and residual SEI. Consequently, a residual tensile strain remains on the Cu foil, preventing full recovery to its initial state, as also exemplified by the low coulombic efficiency. In fact, the strain experienced by the Cu foil originates from volume changes induced by longitudinal lithium deposition at the interface. This lateral strain represents a physical manifestation of longitudinal strain (eqn (1)–(3), SI). Fundamentally, this process reflects how volume expansion of lithium in the thickness direction (*i.e.*, longitudinal) generates detectable strain signals in the lateral direction, which can be reflected in Fig. S3, SI. Through repeated plating/stripping cycling, the strain gauges successfully capture real-time mechanical perturbations arising from non-

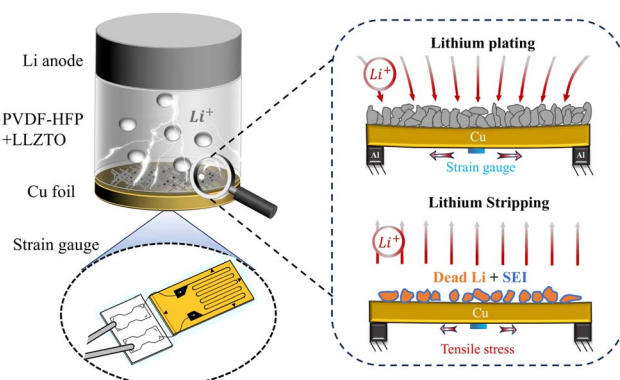


Fig. 1 Mechanism diagram of strain generation at different periods of battery cycling.



uniform lithiation at the interface, providing critical insights into progressive degradation mechanisms.

### Evolution of strain during the cycle of Cu||Li cells

Strain measurements during plating/stripping were conducted on Cu||Li cells under a constant current density of  $0.1 \text{ mA cm}^{-2}$  and an applied stack pressure of 200 KPa. The results revealed a sustained and progressively increasing tensile strain on the Cu foil throughout cycling (Fig. 2a), which can be categorized into three distinct periods, mainly corresponding to specific structural and electrochemical changes within the cell. The identified three characteristic strain evolution periods include initial linear growth, intermediate stabilization, and terminal exponential escalation prior to cell failure. We further examined the representative enlarged plating/stripping cycles (Fig. 2b–d). In the first cycle, there was significant fluctuation in strain values, likely attributable to electrochemical instability present during the initial cycle.<sup>34,35</sup> During the initial linear growth period (2–7 cycles), it is observed that the measured microstrain increases linearly during plating, while subsequent stripping partially releases microstrain during one cycle (Fig. 2b). Both the peak strain (at the end of plating) and the residual strain (after stripping) increased nearly linearly during this period.

After 7 cycles, the end-of-cycle strain surges from  $0.6 \mu\epsilon$  to  $138.4 \mu\epsilon$ . This rapid rise is mainly attributed to the tremendous irreversible reactions with formation of an SEI to gradually stabilize the interfaces. This can be reflected by the low CE values in the initial several cycles, increasing from 57% to 75% (Fig. 2e). In the second period (cycles 8–24), the strain can be almost recovered during each single plating/stripping cycle (Fig. 2c). Consequently, the strain stays steadily without obvious growth during this cycling period, which stabilizes at  $\sim 134.1 \mu\epsilon$  over continues 17 cycles. This presence of plateau suggests a period of relatively reversible Li deposition and stripping with minimized irreversible reactions. Likewise, the corresponding CE stabilizes at  $\sim 76\%$  without fluctuations, coinciding with the strain plateau (Fig. 2e). In the third period (cycles 25–61) over the course of 37 cycles, the strain behavior in each single cycle is similar to the first period (Fig. 2d), and the residual strain increases from  $139 \mu\epsilon$  to  $440 \mu\epsilon$  with final complete failure. Such sustained increase is mainly caused by the intensified inhomogeneity in Li plating/stripping with accumulated dead Li on Cu foil upon continuous cycles, thus giving rise to progressive mechanical degradation. However, the corresponding CE remains quite stable during this period (Fig. 2e), which is mainly due to the excess Li inventory from a thick Li foil

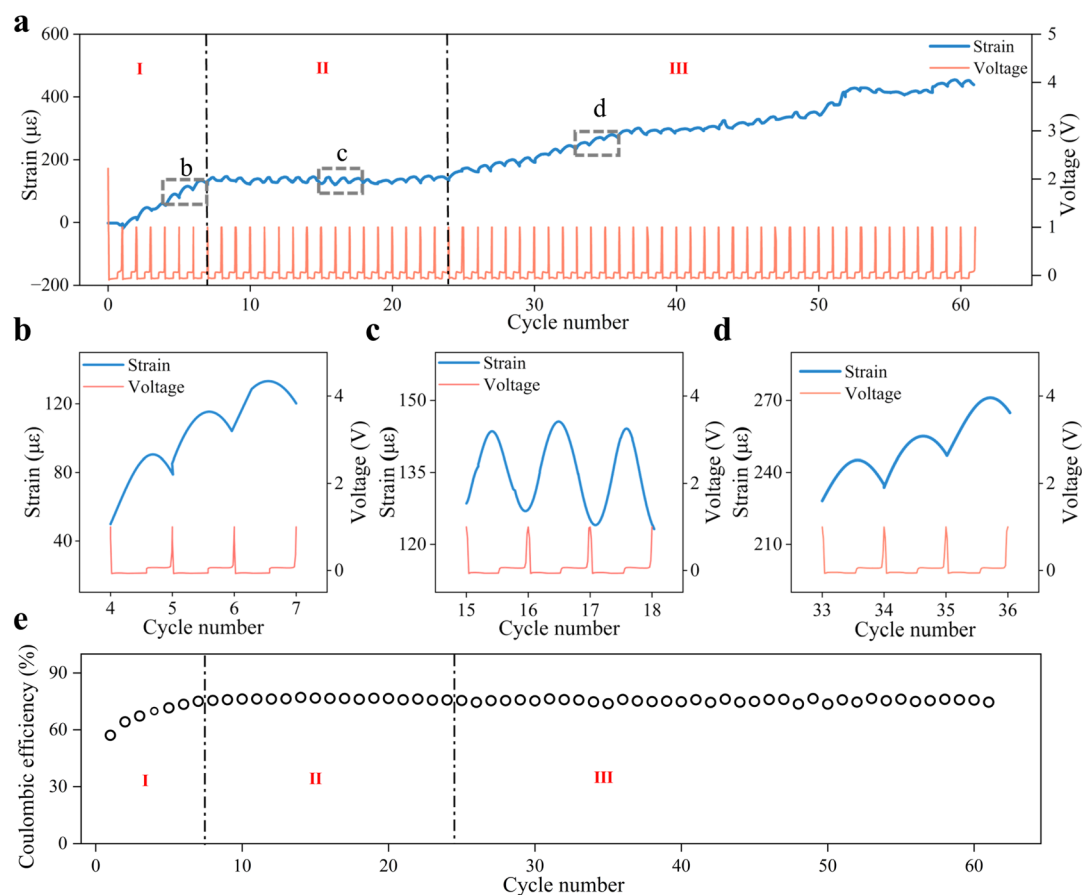


Fig. 2 (a) The evolution of battery voltage and strain as a function of cycle number at a current density of  $0.1 \text{ mA cm}^{-2}$  under an initial stack pressure of 200 KPa. (b) Voltage and strain profiles during cycles 4–7. (c) Voltage and strain profiles during cycles 15–18. (d) Voltage and strain profiles during cycles 33–36. (e) Coulombic efficiency vs. cycle number at a current density of  $0.1 \text{ mA cm}^{-2}$  and initial stack pressure of 200 KPa.

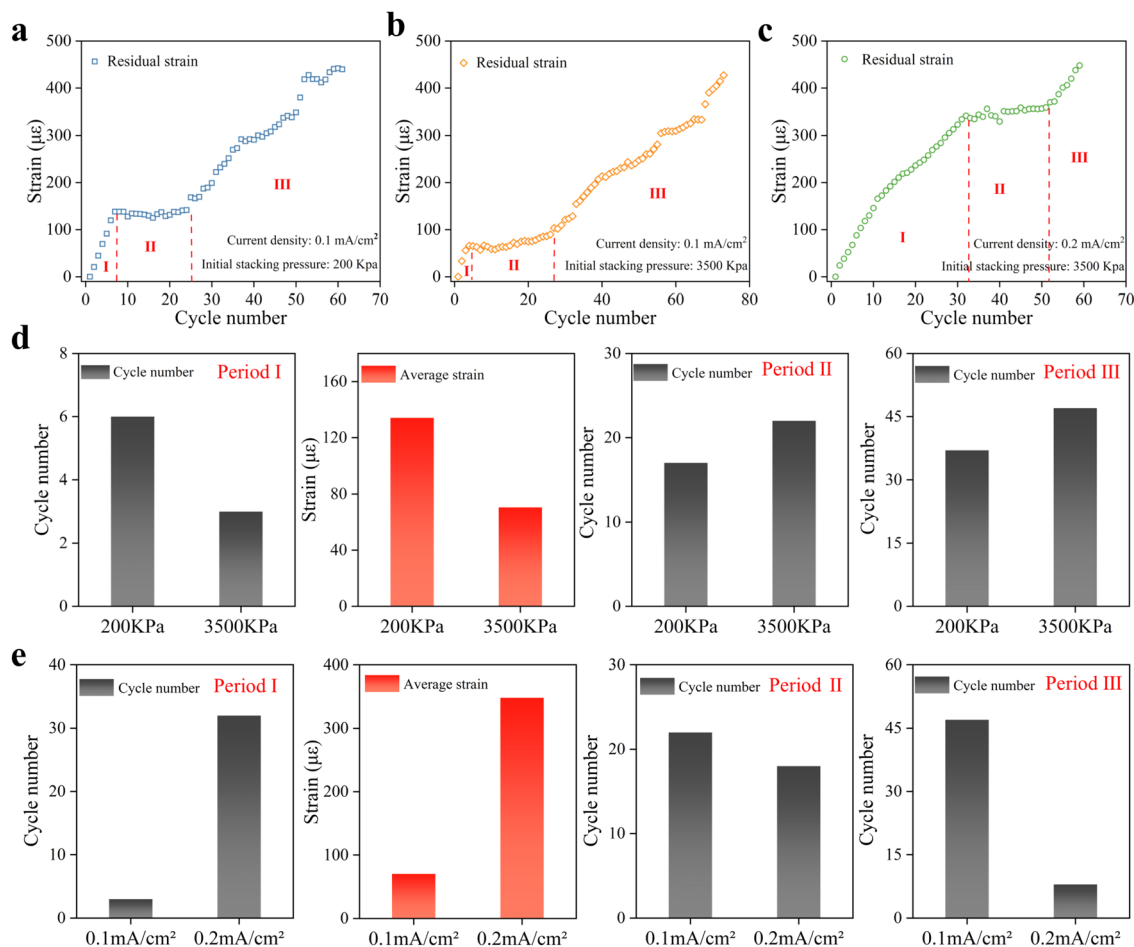


Fig. 3 (a–c) Evolution of residual strain versus cycle number under three distinct operational conditions. (d) Comparative diagrams of the three periods under different pressures. (e) Comparative diagrams of the three periods under different densities.

electrode to continuously compensate for the irreversible Li<sup>+</sup> depletion, leading to artificially improved CE. In fact, the majority of state-of-the-art Li batteries or beyond adopt an excessive amount of Li (or Na) than that actually being cycled, as exemplified by the high negative-to-positive areal capacity.<sup>36–39</sup> Therefore, it is quite unviable to evaluate the cycling failure just from the CE value. In sharp contrast, the *in situ* strain monitoring can reliably diagnose the irreversibility and failure evidence because the sensor solely monitors the Cu foil electrode side with intrinsic mechanical deformation. Collectively, these findings demonstrate a direct relationship between interfacial deformation dynamics and electrochemical behavior, underscoring strain sensing as a powerful diagnostic tool for Li metal batteries.

#### Effect of initial stack pressure and current density on strain evolution

The aforementioned study elucidates the correlation between dynamic strain evolution and electrochemical failure of copper electrodes under constant current density (0.1 mA cm<sup>−2</sup>) and stack pressure (200 KPa) conditions. However, practical operating conditions of lithium metal batteries (*e.g.*, fast charging

and mechanical packaging designs) typically involve much broader ranges of current densities and pressures, while their influences on interfacial mechanical behavior remain unclear. Notably, the initial stack pressure exerts profound impacts on the electro-chemo-mechanical behavior of all-solid-state batteries, particularly in maintaining electrode–electrolyte interfacial contact and mitigating degradation.<sup>40</sup> Comparative experiments conducted at pressures of 200 KPa and 3500 KPa (0.1 mA cm<sup>−2</sup>) revealed that the three-period characteristic of strain evolution persists under high pressure, but there exist significant changes in each period (Fig. 3b). At 3500 KPa, the first period was shortened to 3 cycles (Fig. 3d), a reduction of 50% as compared to that of 200 KPa pressure. Meanwhile, there is a slight reduction in the strain accumulation rate (22 με per cycle *vs.* 23.1 με per cycle at 200 KPa). This is because the increased initial pressure accelerates the formation of a stable SEI, thereby reducing the time required to achieve cycling stability. In the second period, the stabilized strain value was significantly lowered by 47.4% (average strain: 70.5 με *vs.* 134.1 με at 200 KPa, Fig. 3b and d). During the third period, the strain growth rate decreases from 7.3 με per cycle at 200 KPa to 6.9 με per cycle, indicating a further reduction in plating/stripping





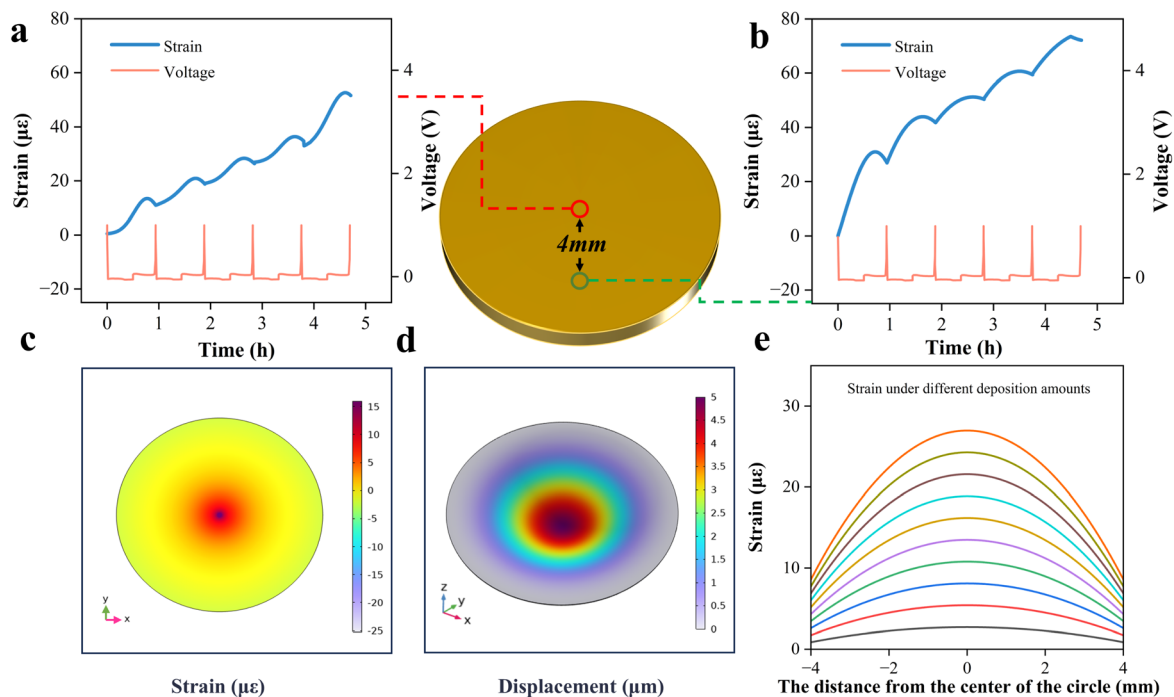


Fig. 4 (a) Strain and voltage vs. time at the center of the electrode. (b) Strain and voltage vs. time at the edge of the electrode. (c) Planar strain distribution contour and (d) spatial displacement contour on the Cu foil assuming a certain amount of Li plated with 15  $\mu\text{e}$ . (e) Strain vs. distance from center profiles under different deposition amounts.

heterogeneity induced by the elevated pressure. Cross-referencing the coulombic efficiency curve (Fig. S4) at 0.1 mA  $\text{cm}^{-2}$  and 3500 KPa initial stacking pressure with its cyclic strain profile reveals the following: Stage I shows progressive CE increase alongside acute cyclic strain surge; Stage II exhibits stable CE with negligible strain growth, consistent with the strain plateau; while Stage III demonstrates continuous strain accumulation despite the marginal CE decay, invalidating CE-based failure assessment. In summary, increasing the stacking pressure from 200 KPa to 3500 KPa cuts the initial strain growth cycle and lowers the average stabilized strain value, while prolonging the battery life. These results prove the pressure-dependent suppression of mechanical degradation.

In addition to stacking pressure, the effects of plating/stripping rates (*i.e.*, charge/discharge capabilities) were examined, as these are critical for high-power performance.<sup>41</sup> The influence of current density was investigated by increasing it from 0.1 to 0.2 mA  $\text{cm}^{-2}$ , which dramatically altered the strain evolution profile (Fig. 3c). Under the current density of 0.2 mA  $\text{cm}^{-2}$ , the first period duration increased substantially. This resulted in a markedly higher strain value when reaching the plateau stage (second period), with an average strain of 348.2  $\mu\epsilon$ . The third period ended prematurely after only 8 cycles, leading to reduced battery cycle life. Among them, the strain growth rates at different periods are shown in Fig. S5. Elevated current densities induce persistent strain escalation from initial cycles accompanied by monotonic CE decline (Fig. S6). Comparatively, doubling the current density increased the initial strain growth duration by 10 times and increased the average plateau strain by

4 times, significantly shortening the cycle life. This transition reflects the dominance of kinetic effects at higher current densities, where enhanced  $\text{Li}^+$  concentration gradients and preferential dendrite initiation at surface defects<sup>42</sup> accelerate mechanical degradation.

These findings highlight two critical optimization parameters for Li metal batteries: (1) the stack pressure should be optimized to minimize the first-period duration while maximizing the second-period stability and (2) the current density must be carefully selected to balance power requirements with mechanical stability. The strain monitoring system demonstrated excellent sensitivity to both parameters, proving capable of detecting subtle mechanical changes associated with different operating conditions while maintaining robust identification capabilities even at elevated current densities.

### Spatial evolution of strain across the electrode surface

To gain a comprehensive understanding of the spatial strain distribution across the electrode, strain gauges were strategically bonded to distinct locations on the copper foil, with a 4 mm spacing between adjacent sensors, as illustrated in Fig. 4a and b. A notable spatial dependence of strain evolution was observed: strain magnitudes decreased progressively from the central region toward the periphery, accompanied by slower strain accumulation rates at edge locations. Quantitative analysis revealed distinct mechanical behaviors: (1) central region: the final strain increased from 0 to 72.15  $\mu\epsilon$  over the first five cycles, yielding an average strain increment of 14.43  $\mu\epsilon$  per cycle; (2) edge region: the final strain reached 51.66  $\mu\epsilon$  under



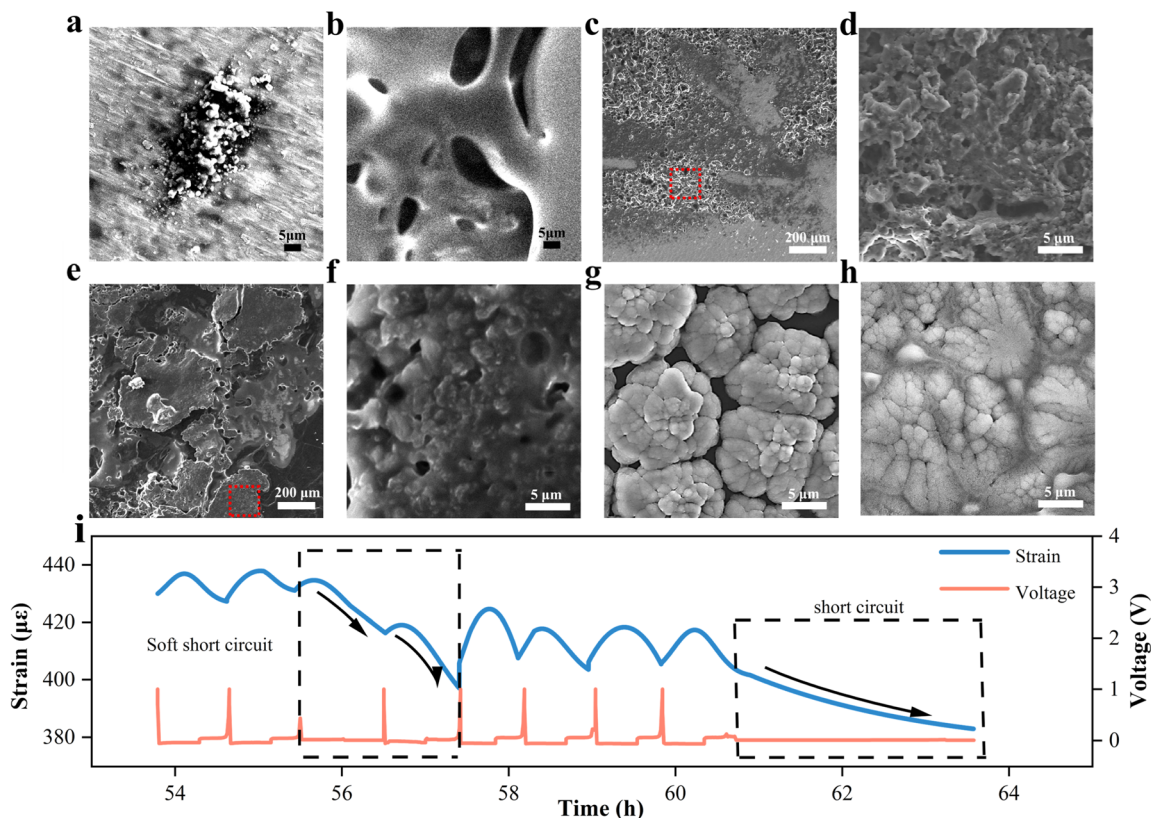


Fig. 5 (a) SEM image of the Cu foil surface after 5 plating/stripping cycles. (b) SEM image of the Cu foil surface after 15 plating/stripping cycles. (c) SEM image of the Cu foil surface after 30 stripping cycles and (d) the corresponding high-magnification view of the red-outlined region. (e) SEM image of the Li electrode surface after 30 plating/stripping cycles and (f) the corresponding high-magnification view of the red-outlined region. (g) SEM image of Li deposition under an initial stack pressure of 200 KPa. (h) SEM image of lithium deposition under an initial stack pressure of 3500 KPa. (i) Temporal evolution of strain and voltage prior to battery failure under  $0.2 \text{ mA cm}^{-2}$  current density and 3500 KPa initial stack pressure.

identical cycling conditions, corresponding to a lower average rate of  $10.33 \mu\epsilon$  per cycle. It should be noted that the edge region of the Cu foil was partially constrained by the surrounding PTFE mold to ensure structural stability. Although this constraint may locally alter the mechanical boundary conditions and reduce the strain response magnitude, the strain gauges adhered in both central and edge positions still captured meaningful relative variations.

We employed finite element analysis software (COMSOL Multiphysics) to further elucidate the non-uniform strain distribution on electrodes during plating/stripping processes. The hygroscopic swelling module was adopted to simulate battery plating behavior. The simulation results further validate the spatial gradient distribution of strain (Fig. 4c and d). Furthermore, strain distributions corresponding to different deposition amounts are presented in Fig. 4e, revealing a distinct nonlinear relationship between strain magnitude and distance from the center. This strain gradient is fundamentally attributed to pressure distribution heterogeneity induced by the variations in stack pressure. The presence of a circular ring at the edge of the copper foil results in a progressive reduction of surface pressure from the edge toward the center. Higher stack pressure partially suppresses irreversible volume expansion

caused by dendrites, dead lithium, and fractured SEI, ultimately leading to lower strain generation at the electrode edge compared to the central region.

### Battery failure analysis

Post-mortem examination of cycled cells revealed that during the initial cycling stage (Fig. 5a), mossy lithium dendrites emerged and accumulated on the copper foil surface, forming a rough, porous structure that contributed to progressive strain buildup. Upon entering the mid-cycling phase, discrete dendrites coalesced into interconnected networks (Fig. 5b), creating a porous flake-like morphology with relatively smooth surfaces. Both the SEI layer and dendrite structures stabilized during this plateau period, resulting in negligible strain growth. XPS quantification of SEI evolution from the initial to mid-cycling stages (Table S1) demonstrated a compositional transition: from organic-dominated SEI (93.91 at% C, 5.95 at% O, and 0.14 at% F) in early cycles toward inorganic-rich constituents (28.61 at% C, 46.02 at% O, and 25.37 at% F) at stabilization. This matured SEI contributed marginally to the overall strain accumulation. During later cycling stages (after 30 cycles, Fig. 5c and d), severe Li dendrite formation and “dead Li” accumulation were observed on the Cu foil. The Li anode surface also



exhibited nonuniform plating, with grayish-white regions covered by porous SEI shells (Fig. 5e and f). These structural defects contributed to irreversible electrode thickening, elevating the residual strain and internal cell pressure with each cycle. Meanwhile, the morphology of Li deposition under different initial stacking pressures is shown in Fig. 5g and h. Under high initial stacking pressure, Li deposition appears more compact with reduced porosity, resulting in a thinner electrode thickness. This indicates that the pressure effect predominantly influences the early stages of Li nucleation and growth, specifically during the first stress change period.

The strain evolution characteristics during battery short-circuit were systematically investigated, as shown in Fig. 5i. When the cell entered the final stage of the third period under  $0.2 \text{ mA cm}^{-2}$  current density and 3500 KPa stack pressure, the accumulated effects of dendrite growth, dead lithium formation, and intensified side reactions eventually caused the composite solid-state electrolyte membrane to fail. After 55 charge–discharge cycles, the voltage profile exhibited a sudden and dramatic polarization drop due to the formation and dissolution of micro-dendrites, indicating the occurrence of soft short-circuit.<sup>32,33</sup> During this event, the charge/discharge voltage approached near-zero levels while the strain rapidly decreased from  $431.1 \mu\epsilon$  to  $398.8 \mu\epsilon$ , with this abnormal state persisting for two complete cycles before temporary recovery. The cell experienced complete short-circuit at the 60th cycle (strain value:  $404.2 \mu\epsilon$ ), where the strain reduction was attributed to internal electrolyte damage leading to structural integrity loss and consequent stress relaxation.

Remarkably, comparative analysis under various conditions revealed that the final strain values during short-circuit events consistently stabilized around  $400 \mu\epsilon$ , suggesting that this value represents the strain tolerance limit of the PVDF-HFP/LLZTO composite electrolyte. This finding provides critical insights for battery safety management, as it establishes a quantitative mechanical threshold for failure prediction. While soft short-circuits are typically attributed to preferential Li growth along LLZTO grain boundaries,<sup>43–45</sup> in polymer-based solid electrolytes, the penetration of Li along LLZTO grain boundaries at the interface seems quite low. The chance of failure mechanism of soft short-circuiting is a quite interesting topic, which will be a subject worthy of further investigation using ceramic-based solid-state electrolytes. The strain monitoring technique demonstrates superior sensitivity compared to conventional voltage-based methods, particularly in detecting soft short-circuit events that often precede catastrophic failure. These results highlight the importance of real-time mechanical monitoring for early failure detection in solid-state battery systems. The observed correlation between mechanical strain evolution and electrical failure modes offers new perspectives for developing more robust electrolyte materials and advanced battery management strategies.

### Cycling stress calculation

Finite element simulations were performed using COMSOL Multiphysics to investigate the internal stress–strain

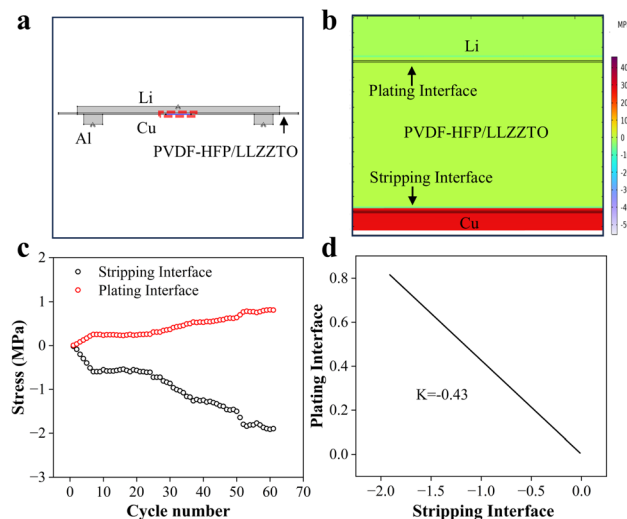


Fig. 6 (a) Simulation of the equivalent battery. (b) Simulation results of the internal structural stresses in the battery when the short-circuit occurs in the battery. (c) Stress change curves at the plating and stripping interfaces during battery cycling. (d) The variation curve of plating interface stress with stripping interface stress.

distribution during battery cycling. The computational model accurately represents the experimental cell configuration (Fig. 6a), incorporating a PVDF-HFP/LLZTO composite electrolyte modeled as an isotropic elastic solid with a Young's modulus of 60 MPa and tensile strength of 13.2 MPa.<sup>46</sup> The stresses generated during the entire cycle arose from significant volume changes of the Li metal during plating and stripping ( $1 \text{ mA h cm}^{-2} \approx 5 \mu\text{m}$ ).<sup>47–49</sup> We established a  $0.1 \mu\text{m}$  plating layer at the Cu foil/electrolyte interface and employed the hygroscopic swelling module to simulate the effects of Li plating. Roller-supported boundary conditions were applied to both the electrode and Al ring, while boundary probes at strain gauge locations enabled direct comparison with experimental measurements.

The simulation results demonstrated that stress evolution during cycling followed patterns consistent with experimental strain gauge measurements, though with significant differences in magnitude. After one complete cycle, the model predicted 2.84 MPa stress ( $23 \mu\epsilon$  strain) on the Cu foil, compared to 0.04 MPa and  $-0.1 \text{ MPa}$  at the plating and stripping interfaces, respectively. The stress on the Cu foil reached 49.5 MPa ( $400.4 \mu\epsilon$ ) at battery failure. While the interface stresses reaching 0.74 MPa (plating) and  $-1.73 \text{ MPa}$  (stripping), as shown in Fig. 6b and c. The slightly lower stress value at the plating interface reflects stress absorption by the electrolyte (Fig. 6d).

The analysis highlights two critical phenomena: (1) the electrolyte's significant role in stress redistribution and (2) the cumulative effect of irreversible deformation during cycling, where decreasing Li utilization leads to progressively increasing interfacial stresses. This stress accumulation ultimately exceeds the electrolyte's mechanical tolerance, contributing to cell failure. These findings provide quantitative insights into the mechanical degradation mechanisms of solid-state batteries





and demonstrate the value of coupled experimental simulation approaches for battery performance analysis. The established correlation between simulated stresses and measured strains offer a powerful tool for predicting the battery lifetime and optimizing mechanical design parameters.

## Conclusions

This study systematically investigates the electrochemical-mechanical coupling behavior in solid-state lithium metal batteries through an innovative strain monitoring approach, revealing three distinct stages of strain evolution with characteristic growth rates that are critically influenced by operational parameters. Increasing the stack pressure from 200 KPa to 3500 KPa produces a 50% reduction in initial strain growth duration and 47.4% decrease in plateau strain while extending the cycle life, whereas doubling the current density causes a 10-fold prolongation of initial strain growth and 4-fold increase in plateau strain with significant cycle life reduction. The research establishes correlations between mechanical strain evolution and electrochemical performance throughout cycling while simultaneously characterizing the spatial development of electrode surface strains. Finite element simulations further elucidate the internal stress-strain distributions by accounting for electrolyte-mediated effects, providing mechanistic insights into interfacial deformation processes. This work provides both a fundamental understanding of pressure and current dependent degradation mechanisms and practical tools for battery performance optimization.

## Author contributions

H. Zhang: data curation, formal analysis, investigation, visualization, writing – original draft. Z. Chen: software, data curation, methodology. X. Zhang: supervision, validation, writing – review & editing. Z. Shen: project administration, visualization. F. Xu: resources, supervision, funding acquisition, visualization, writing – review & editing. F. Wang: conceptualization, funding acquisition, investigation, resources, supervision, writing – review & editing.

## Conflicts of interest

The authors declare no competing financial interests.

## Data availability

The data supporting this article have been included as part of the SI.

Supplementary information is available. See DOI: <https://doi.org/10.1039/d5sc03046c>.

## Acknowledgements

This work was supported by the National Natural Science Foundation of China (52322203 and 52473220) and the Fundamental Research Funds for the Central Universities.

## Notes and references

- 1 M. Armand and J. M. Tarascon, Building better batteries, *Nature*, 2008, **451**, 652–657.
- 2 X. Zhang, X. Cheng and Q. Zhang, Nanostructured energy materials for electrochemical energy conversion and storage: A review, *J. Energy Chem.*, 2016, **25**, 967–984.
- 3 L.-Z. Fan, H. He and C.-W. Nan, Tailoring inorganic-polymer composites for the mass production of solid-state batteries, *Nat. Rev. Mater.*, 2021, **6**, 1003–1019.
- 4 A. M. Abakumov, S. S. Fedotov, E. V. Antipov and J. M. Tarascon, Solid state chemistry for developing better metal-ion batteries, *Nat. Commun.*, 2020, **11**, 4976.
- 5 S. Randau, D. A. Weber, O. Kötz, R. Koerver, P. Braun, A. Weber, E. Ivers-Tiffée, T. Adermann, J. Kulisch, W. G. Zeier, F. H. Richter and J. Janek, Benchmarking the performance of all-solid-state lithium batteries, *Nat. Energy*, 2020, **5**, 259–270.
- 6 H. Wu, H. Jia, C. Wang, J. G. Zhang and W. Xu, Recent progress in understanding solid electrolyte interphase on lithium metal anodes, *Adv. Energy Mater.*, 2020, **11**, 2003092.
- 7 W.-W. Wang, Y. Gu, C.-X. Liu, J. Yan and B.-W. Mao, Exploring the role of LiI additive in regulating the morphology of lithium deposition by *in situ* AFM, *J. Phys. Chem. C*, 2023, **127**, 12492–12501.
- 8 C. Fang, X. Wang and Y. S. Meng, Key issues hindering a practical lithium-metal anode, *Trends Chem.*, 2019, **1**, 152–158.
- 9 W. Xu, J. Wang, F. Ding, X. Chen, E. Nasybulin, Y. Zhang and J.-G. Zhang, Lithium metal anodes for rechargeable batteries, *Energy Environ. Sci.*, 2014, **7**, 513–537.
- 10 R. Yao, Z. Li, L. Bao, R. Deng, K. Zheng, Y. Hu, J. Li, H. Zhang, S. Tu, R. Shi, J. Wu, C. Li and X. Liu, Superior stability of Li<sub>5</sub>Mg@Cu anodes for lithium metal batteries: Investigating the suppression effects of magnesium on lithium dendrite growth, *J. Mater. Sci. Technol.*, 2025, **211**, 288–302.
- 11 K. J. Kim, M. Balaish, M. Wadaguchi, L. Kong and J. L. M. Rupp, Solid-state Li-metal batteries: challenges and horizons of oxide and sulfide solid electrolytes and their interfaces, *Adv. Energy Mater.*, 2020, **11**, 2002689.
- 12 B. Ozdogru, S. Padwal, B. Bal, S. Harimkar, B. Koohbor and Ö. Ö. Çapraz, Coupling between voltage profiles and mechanical deformations in LAGP solid electrolyte during Li plating and stripping, *ACS Appl. Energy Mater.*, 2022, **5**, 2655–2662.
- 13 J. A. Lewis, J. Tipples, F. J. Q. Cortes and M. T. McDowell, Chemo-mechanical challenges in solid-state batteries, *Trends Chem.*, 2019, **1**, 845–857.
- 14 Z. Zheng, X. Fang, W. Deng, P. Li, X. Zheng, H. Zhang, L. Li, S. Chou, Y. Chen, Y. Tang and J. Wang, Quantitatively detecting and characterizing metallic lithium in lithium-based batteries, *Energy Environ. Sci.*, 2024, **17**, 9051–9092.
- 15 L. Porz, T. Swamy, B. W. Sheldon, D. Rettenwander, T. Frömling, H. L. Thaman, S. Berendts, R. Uecker, W. C. Carter and Y. M. Chiang, Mechanism of lithium





- metal penetration through inorganic solid electrolytes, *Adv. Energy Mater.*, 2017, 7, 1701003.
- 16 E. Kazyak, R. Garcia-Mendez, W. S. LePage, A. Sharafi, A. L. Davis, A. J. Sanchez, K.-H. Chen, C. Haslam, J. Sakamoto and N. P. Dasgupta, Li penetration in ceramic solid electrolytes: operando microscopy analysis of morphology, propagation, and reversibility, *Matter*, 2020, 2, 1025–1048.
  - 17 H. Zhang, X. Zhang, Z. Shen, X. Peng, F. Wang, F. Xu and X. Zhao, Ultrasound overcomes dendrite puncture in Li metal batteries, *J. Energy Storage*, 2024, 85, 110976.
  - 18 F. Xia, W. Zeng, H. Peng, H. Wang, C. Sun, J. Zou and J. Wu, Revealing structural degradation in layered structure oxides cathode of lithium ion batteries *via in situ* transmission electron microscopy, *J. Mater. Sci. Technol.*, 2023, 154, 189–201.
  - 19 K. J. Harry, D. T. Hallinan, D. Y. Parkinson, A. A. MacDowell and N. P. Balsara, Detection of subsurface structures underneath dendrites formed on cycled lithium metal electrodes, *Nat. Mater.*, 2014, 13, 69–73.
  - 20 Y.-C. Hsieh, J. H. Thienenkamp, C.-J. Huang, H.-C. Tao, U. Rodehorst, B. J. Hwang, M. Winter and G. Brunklaus, Revealing the impact of film-forming electrolyte additives on lithium metal batteries *via* solid-state NMR/MRI analysis, *J. Phys. Chem. C*, 2021, 125, 252–265.
  - 21 F. Shi, A. Pei, A. Vailionis, J. Xie, B. Liu, J. Zhao, Y. Gong and Y. Cui, Strong texturing of lithium metal in batteries, *Proc. Natl. Acad. Sci. U. S. A.*, 2017, 114, 12138–12143.
  - 22 S. Lv, T. Verhallen, A. Vasileiadis, F. Ooms, Y. Xu, Z. Li, Z. Li and M. Wagemaker, Operando monitoring the lithium spatial distribution of lithium metal anodes, *Nat. Commun.*, 2018, 9, 2152.
  - 23 W. Huang, Y. Ye, H. Chen, R. A. Vilá, A. Xiang, H. Wang, F. Liu, Z. Yu, J. Xu, Z. Zhang, R. Xu, Y. Wu, L.-Y. Chou, H. Wang, J. Xu, D. T. Boyle, Y. Li and Y. Cui, Onboard early detection and mitigation of lithium plating in fast-charging batteries, *Nat. Commun.*, 2022, 13, 7019.
  - 24 Z. Miao, Y. Li, X. Xiao, Q. Sun, B. He, X. Chen, Y. Liao, Y. Zhang, L. Yuan, Z. Yan, Z. Li and Y. Huang, Direct optical fiber monitor on stress evolution of the sulfur-based cathodes for lithium–sulfur batteries, *Energy Environ. Sci.*, 2022, 15, 2029–2038.
  - 25 Y. Chang, Y. Cheng, R. Jia, R. Wang, Q. Xu, L. Gong, Y. Wei, B. Tang, C. Guo, B. Sun, X. He, X. Li, L. Gong, H. Ye, X. Wang, Y. Dai, M. Dong, Y. Tang, F. Zhang, P. Tan and T. Pan, Unified iontronic sensing for operando monitoring of physical–chemical events in lithium-ion batteries, *Natl. Sci. Rev.*, 2025, 12, nwaf151.
  - 26 J. Fan, C. Liu, N. Li, L. Yang, X.-G. Yang, B. Dou, S. Hou, X. Feng, H. Jiang, H. Li, W.-L. Song, L. Sun, H.-S. Chen, H. Gao and D. Fang, Wireless transmission of internal hazard signals in Li-ion batteries, *Nature*, 2025, 641, 639–645.
  - 27 Y. Liu, Y. Zhu and Y. Cui, Challenges and opportunities towards fast-charging battery materials, *Nat. Energy*, 2019, 4, 540–550.
  - 28 S. S. Zhang, The effect of the charging protocol on the cycle life of a Li-ion battery, *J. Power Sources*, 2006, 161, 1385–1391.
  - 29 Z.-X. Wang, Y. Lu, C.-Z. Zhao, W.-Z. Huang, X.-Y. Huang, W.-J. Kong, L.-X. Li, Z.-Y. Wang, H. Yuan, J.-Q. Huang and Q. Zhang, Suppressing Li voids in all-solid-state lithium metal batteries through Li diffusion regulation, *Joule*, 2024, 8, 2794–2810.
  - 30 M. Jäckle, K. Helmbrecht, M. Smits, D. Stottmeister and A. Groß, Self-diffusion barriers: possible descriptors for dendrite growth in batteries?, *Energy Environ. Sci.*, 2018, 11, 3400–3407.
  - 31 U. B. W. Frank, C. Elsässer and M. Fähnle, First-principles calculations of absolute concentrations and self-diffusion constants of vacancies in lithium, *Phys. Rev. Lett.*, 1996, 77, 518–521.
  - 32 Y. Lu, C. Z. Zhao, H. Yuan, X. B. Cheng, J. Q. Huang and Q. Zhang, Critical current density in solid-state lithium metal batteries: mechanism, influences, and strategies, *Adv. Funct. Mater.*, 2021, 31, 2009925.
  - 33 V. Raj, V. Venturi, V. R. Kankanallu, B. Kuiri, V. Viswanathan and N. P. B. Aetukuri, Direct correlation between void formation and lithium dendrite growth in solid-state electrolytes with interlayers, *Nat. Mater.*, 2022, 21, 1050–1056.
  - 34 J. P. Vivek and N. Garcia-Araez, Differences in interfacial reactivity of graphite and lithium metal battery electrodes investigated *via operando* gas analysis, *J. Phys. Chem. C*, 2024, 128, 13395–13401.
  - 35 C. Wang, F. Yang, W. Wan, S. Wang, Y. Zhang, Y. Huang and J. Li, A large-area lithium metal–carbon nanotube film for precise contact prelithiation in lithium-ion batteries, *Energy Environ. Sci.*, 2023, 16, 4660–4669.
  - 36 Y. Su, F. Xu, X. Zhang, Y. Qiu and H. Wang, Rational Design of High-Performance PEO/Ceramic Composite Solid Electrolytes for Lithium Metal Batteries, *Nano-Micro Lett.*, 2023, 15, 82.
  - 37 X. Z. Rong Zhuang, C. Qu, X. Xu, J. Yang, Q. Ye, Z. Liu, S. Kaskel, F. Xu and H. Wang, Fluorinated porous frameworks enable robust anode-less sodium metal batteries, *Sci. Adv.*, 2023, 9, eadh8060.
  - 38 C. Q. Fei Xu, Q. Lu, J. Meng, X. Zhang, X. Xu, Y. Qiu, B. Ding, J. Yang, F. Cao, P. Yang, G. Jiang, S. Kaskel, J. Ma, L. Li, X. Zhang and H. Wang, Atomic Sn-enabled high-utilization, large-capacity, and long-life Na anode, *Sci. Adv.*, 2022, 8, eabm748.
  - 39 Y. S. Jinbo Zhang, Y. Qiu, X. Zhang, F. Xu and H. Wang, High-Strength, thin, and lightweight solid polymer electrolyte for superior all-solid-state sodium metal batteries, *ACS Appl. Mater. Interfaces*, 2024, 16, 30128–30136.
  - 40 J. Sang, B. Tang, Y. Qiu, Y. Fang, K. Pan and Z. Zhou, How does stacking pressure affect the performance of solid electrolytes and all-solid-state lithium metal batteries?, *Energy Environ. Mater.*, 2023, 7, e12670.
  - 41 J. Zheng, M. H. Engelhard, D. Mei, S. Jiao, B. J. Polzin, J.-G. Zhang and W. Xu, Electrolyte additive enabled fast charging and stable cycling lithium metal batteries, *Nat. Energy*, 2017, 2, 17012.



- 42 P. Shi, X. B. Cheng, T. Li, R. Zhang, H. Liu, C. Yan, X. Q. Zhang, J. Q. Huang and Q. Zhang, Electrochemical diagram of an ultrathin lithium metal anode in pouch cells, *Adv. Mater.*, 2019, **31**, 1902785.
- 43 Y. Ren, Y. Shen, Y. Lin and C.-W. Nan, Direct observation of lithium dendrites inside garnet-type lithium-ion solid electrolyte, *Electrochem. Commun.*, 2015, **57**, 27–30.
- 44 L. E. Marbella, S. Zekoll, J. Kasemchainan, S. P. Emge, P. G. Bruce and C. P. Grey, <sup>7</sup>Li NMR Chemical Shift Imaging To Detect Microstructural Growth of Lithium in All-Solid-State Batteries, *Chem. Mater.*, 2019, **31**, 2762–2769.
- 45 E. J. Cheng, A. Sharafi and J. Sakamoto, Intergranular Li metal propagation through polycrystalline Li<sub>6.25</sub>Al<sub>0.25</sub>La<sub>3</sub>Zr<sub>2</sub>O<sub>12</sub> ceramic electrolyte, *Electrochim. Acta*, 2017, **223**, 85–91.
- 46 Y. Gu, S. She, Z. Hong, Y. Huang and Y. Wu, Enabling lithium metal battery with flexible polymer/garnet type solid oxide composite electrolyte, *Solid State Ionics*, 2021, **368**, 115710.
- 47 S.-Y. Ham, H. Yang, O. Nunez-cuacuas, D. H. S. Tan, Y.-T. Chen, G. Deysher, A. Cronk, P. Ridley, J.-M. Doux, E. A. Wu, J. Jang and Y. S. Meng, Assessing the critical current density of all-solid-state Li metal symmetric and full cells, *Energy Storage Mater.*, 2023, **55**, 455–462.
- 48 S. Chen, C. Niu, H. Lee, Q. Li, L. Yu, W. Xu, J.-G. Zhang, E. J. Dufek, M. S. Whittingham, S. Meng, J. Xiao and J. Liu, Critical parameters for evaluating coin cells and pouch cells of rechargeable Li-metal batteries, *Joule*, 2019, **3**, 1094–1105.
- 49 D. P. Wilkinson and D. Wainwright, *In situ* study of electrode stack growth in rechargeable cells at constant pressure, *J. Electroanal. Chem.*, 1993, **355**, 193–203.

